

Autonomous Safe Landing Site Detection for a Future Mars Science Helicopter

Roland Brockers, Jeff Delaune, Pedro Proen  a, Pascal Schoppmann, Matthias Domnik,
Gerik Kubiak, and Theodore Tzanatos

Jet Propulsion Laboratory / California Institute of Technology

4800 Oak Grove Dr., Pasadena, CA 91109

{brockers, jeff.h.delaune, pproenca, pascal.schoppmann, matthias.domnik,
gerik.kubiak, theodore.tzanatos}@jpl.nasa.gov

Abstract—Future Mars Rotorcrafts require advanced navigation capabilities to enable all terrain access for science investigations with long distance flights that are executed fully autonomously. A critical component is the ability to safely land in hazardous terrain as part of a mission, or triggered by an emergency situation. In this paper, we present an advanced navigation system for continuous on-board terrain reconstruction for the purpose of hazard-free landing site detection for the autonomous navigation of a Mars Science Helicopter - a JPL research concept that investigates the feasibility of flying a multi-kilogram science payload at various Mars science locations, with flight ranges of multiple kilometers per flight. Our approach builds on a vision-based perception system that incorporates an on-board visual-inertial state estimator augmented by a laser altimeter (range-VIO), and a structure-from-motion 3D reconstruction approach that uses a single, downward-looking camera to provide dense depth measurements while the vehicle is in motion. Depth measurements are accumulated in a local, robot-centric, multi-resolution elevation map that is analyzed by a landing site detector to extract safe landing areas below the rotorcraft, based on a heuristic that includes slope, roughness and the presence of landing hazards. Detected landing sites are prioritized by an on-board autonomy engine that either selects suitable landing sites for immediate landing maneuvers, or can explore a terrain location as part of a mission in order to find a best landing site in a pre-planned area. We demonstrate and evaluate our approach on simulated data and data acquired with a surrogate unmanned aerial system (UAS) executing flights over relevant terrain.

TABLE OF CONTENTS

1. INTRODUCTION.....	1
2. A FUTURE MARS SCIENCE HELICOPTER	1
3. RELATED WORK	2
4. 3D PERCEPTION OVER COMPLEX TERRAIN	2
5. TERRAIN MAPPING	3
6. FINDING SUITABLE LANDING SITES.....	4
7. EXPERIMENTAL EVALUATION	5
8. CONCLUSIONS AND FUTURE WORK	6
ACKNOWLEDGMENTS	7
REFERENCES	7
BIOGRAPHY	7

1. INTRODUCTION

Perseverance, NASA’s newest rover which is on its way to Mars, is carrying a technology demonstrator on-board that could enable a new era of Mars exploration: the Mars Helicopter *Ingenuity*. If successful, *Ingenuity* will not only demonstrate the first powered flight on another planet, it also will have to perform its flights completely autonomous, since signal delays between Mars and Earth prevent human interaction during flight. Both aspects could revolutionize Mars exploration. A helicopter would enable access to areas out of reach for rovers, and enable regional-scale science exploration [1]. Additionally, the required, unprecedented level of autonomous mobility is likely to transfer to other missions as well.

While *Ingenuity* is designed to perform a sequence of demonstration flights over benign, flat and level terrain [2], [3], [4], a potential future *Mars Science Helicopter* requires the ability to fly over any type of topography to access science locations in complex 3D terrain. Flights over 3D terrain, on the other hand, require an autonomous safe landing capability that includes landing hazard detection, since existing terrain maps, e.g. derived from HiRISE orbital images, do not have the required resolution to resolve all landing hazards, and landing maneuvers in emergency situations might need to be executed at any time during flight.

A major limitation for implementing a landing hazard detection method are size, weight and power (SWaP) constraints, due to the limited payload capability in Martian atmosphere. Therefore, 3D reconstruction methods compatible with small, lightweight and power-efficient sensors are preferred, and algorithms for landing site detection need to be efficient enough to be executed in near real-time on an embedded computer with limited computational resources.

2. A FUTURE MARS SCIENCE HELICOPTER

Mars Science Helicopter (MSH) is a JPL concept designed to succeed the Mars Helicopter *Ingenuity* to be the first aerial exploration platform on Mars. MSH currently envisions a science payload between 1 and 5 kg, depending on the vehicle variant chosen, and other mission parameters, such as a flight range of up to 25 km at up to 100 m altitude, or additional hover time of up to 8 minutes for science data acquisitions. The currently anticipated MSH avionics hardware follows the Mars Helicopter avionics concept with an upgraded navigation processor, with capabilities similar to

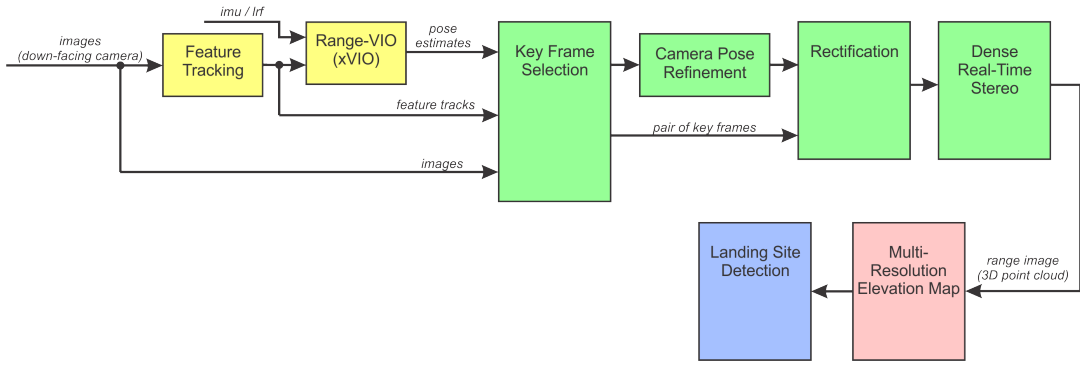


Figure 1. Overview of our complete navigation software. Yellow: leveraged state estimator functions; Green: 3D reconstruction; Red & Blue: landing site detection.

a Qualcomm Snapdragon 820 or 855 SoC.

Potential deployment scenarios are collecting samples from sensitive areas on Mars, autonomous meso-scale mapping, atmospheric sampling, cave exploration, or cliff-wall imaging and interaction [1]. Any MSH mission designed to address a specific scientific need will require the capability to autonomously identify and land on safe landing sites.

3. RELATED WORK

Safe landing site detection for autonomous landing has been pioneered in a number of approaches. NASA developed autonomous landing hazard avoidance for spacecraft landing, initially for landing on the Moon which included a Lidar for 3D perception of landing hazards [5]. Another variant is now deployed on Mars 2020 as the lander vision system (LVS) [6] to support safe landing. LVS uses a monocular camera to estimate spacecraft position during descent with respect to an on-board map with hazard locations predetermined, to diverge the landing trajectory if a landing hazard is present. Unfortunately, size, weight and power constraints prevent the use of a Lidar on a Mars Rotorcraft, and maps with the resolution required to detect landing hazards for rotorcrafts up front are not available (HiRISE's best resolution is ~ 25 cm/pixel).

A number of research approaches use vision-based methods to reconstruct the 3D structure of the overflown terrain based on images from a monocular camera. These approaches couple the reconstruction problem with the state estimation problem and mainly focus on Simultaneous Localization and Mapping (SLAM) [7], [8]. While this is relevant for our approach, our state estimator is a stand alone module for robustness purposes, and for computational efficiency.

[9], [10], [11] use the reconstructed surface directly to find landing sites on flat rooftops, deploying a homography strategy which is not feasible over complex 3D terrain. An optical flow based method was introduced in [12] for landing hazard detection on-board a helicopter test bed. While this approach demonstrated the feasibility of on-board detection, the resolution of the 3D reconstruction was reduced significantly to enable on-board execution, and no temporal fusion was implemented.

Several individual approaches for 3D reconstruction and also mapping are relevant for our work [13], [14]. Recently, ETH Zurich published the *Maplap* open source frame work [15] that combines several 3D reconstruction and mapping re-

search algorithms. While these algorithms are relevant, they are computationally too demanding for on-board processing on a small embedded processor. This is also the case for several component approaches which require a high-end GPU for near real-time execution [16], [14].

4. 3D PERCEPTION OVER COMPLEX TERRAIN

Landing site detection in unknown terrain requires a robust method of on-board 3D perception. Since we want to maximize the science payload on MSH, we couple our 3D reconstruction approach with the on-board state estimator. This has two advantages: First, we can reuse sensor data such as imagery from a down-facing navigation camera for 3D reconstruction. Second, outputs from the estimator can directly be used as pose priors for a structure-from-motion approach, which reduces the computational cost of necessary camera pose reconstruction within the structure-from-motion approach compared to conventional vision-only approaches.

Figure 1 gives an overview of our integrated processing pipeline. Images from the down-facing navigation camera are passed to a feature tracking module to perform frame to frame feature tracking, and as raw data to the structure from motion process (green boxes). The state estimator *xVIO* fuses measurements from feature observations and data from the on-board IMU and a laser range finder (LRF) in a tightly coupled approach [17]. By incorporating the metric information from the LRF, *xVIO* overcomes traditional weaknesses of VIO such as the unobservable metric scale during zero or constant acceleration. This is implemented in a range-facet approach to regain metric scale on triangulated feature observations that can adapt to any terrain topography. This approach guarantees stable pose estimates during critical maneuvers, such as hovering with no motion, and straight line, constant speed trajectories, while providing state of the art accuracy with an average position error of 0.5% of distance traveled and 2° (3σ) global attitude error in roll and pitch in the absence of inertial excitation. While these error levels are accurate enough for controlling the vehicle, they are not sufficient for 3D reconstruction. Therefore, we deploy a camera pose refinement step which executes a windowed bundle adjustment to improve camera poses of selected keyframes and the most recent navigation camera image. Keyframes are stored in a sliding-window, rolling buffer, and are selected based on a parallax constraint, which establishes a minimum and maximum image overlap threshold for a simulated fronto-parallel plane at the distance of the

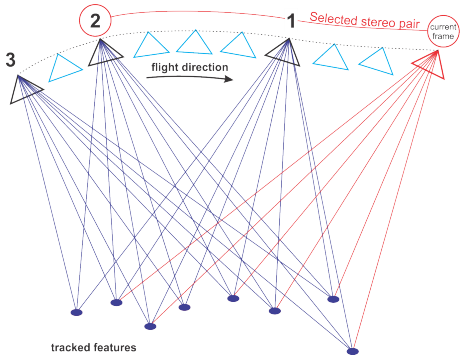


Figure 2. Keyframe approach and stereo frame selection. Poses of the current frame and previous keyframes are optimized during the camera pose refinement step. A keyframe is selected to form a stereo image pair with the current view.

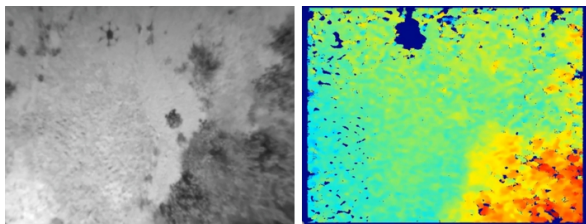


Figure 3. 3D reconstruction example: Left: rectified reference image from UAS flight; Right: reconstructed range image (warm colors are closer to the camera).

overflown terrain (acquired from the LRF), and a minimum number of tracked features constraint, that requires features to be tracked in all keyframes and the current image.

After the refinement step, a past keyframe from the keyframe buffer is selected based on baseline constraints to form a stereo image pair with the current image (Figure 2). Finally, a conventional real-time stereo algorithm [18] is deployed to calculate a dense stereo disparity image which is triangulated into a *range image* to contain the 3D positions of each pixel that was assigned with a valid stereo disparity (Figure 3).

Tying the 3D measurement to the pixel footprint has the advantage that the pixel resolution on the ground can be used to aggregate measurements of similar resolution into a common representation, as will be explained in the next section.

5. TERRAIN MAPPING

3D measurements are processed into a multi-resolution elevation map that is inspired by a Laplacian pyramid structure which doubles the resolution at each consecutive layer (Figure 4). A base layer with the lowest resolution carries the aggregated height estimate for all measurements within the footprint of a cell in this layer, higher resolution layers store the difference between the height estimate at the current layer and the aggregated coarser layers.

This implementation is motivated by two aspects that define the mapping process: The measurement accuracy of the 3D point cloud is directly tied to the pixel footprint on the ground since 3D points were reconstructed by an image based method. Thus, a map representation that can ingest different

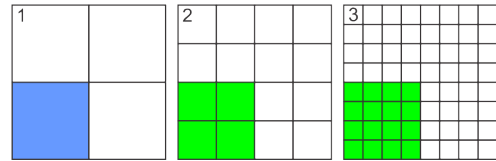


Figure 4. Map resolutions for different layers. Blue: base layer; Green: consecutive layers store residuals. Colored squares in each layer cover the same ground area.

measurement resolutions is preferred. On the other hand, the primary goal for the map implementation is computational efficiency. Therefore, it is desired that landing hazards can be detected at the coarsest resolution possible to save computation time.

The multi-resolution map structure combines the two effects naturally. Following a dynamic Level of Detail (LoD) approach [14] known from Computer Graphics, a new measurement with an assigned resolution (pixel footprint) only has to update the map representation up to the layer that corresponds to its resolution. Finer resolution layers remain untouched. The landing site detector can perform a top down approach to find suitable landing areas. If the terrain at a coarse map resolution already violates the landing constraints, the detection is aborted for this particular area, which leads to a faster execution on average. Further, the process of extracting an elevation map with a desired resolution is simple, since it only involves adding the individual map layers up to the desired resolution (Figure 5).

To limit memory access during map access, we fix the map size in memory, make the map robot-centric and locate the map directly beneath the rotorcraft. When the vehicle moves laterally, the map is moved accordingly by a double rolling buffer implementation, invalidating map cells that move passed the map boundary and adding them in the direction of motion. This leads to an implementation where a map cell with a fixed global position remains at the same location in memory. No resampling is required.

Map updates with new measurements are performed in a coarse to fine strategy. Updates are first applied to the base level, then for each finer level individually. This allows to subtract the current height estimate (aggregated from the coarser levels) from the height measurement to calculate the measurement residual which is then fused with the current layer by a Kalman update, using a measurement variance directly derived from the expected stereo disparity accuracy. In our case, the stereo algorithm provides sub-pixel precise disparity maps, thus we assume a maximum disparity error of 0.25 pixel.

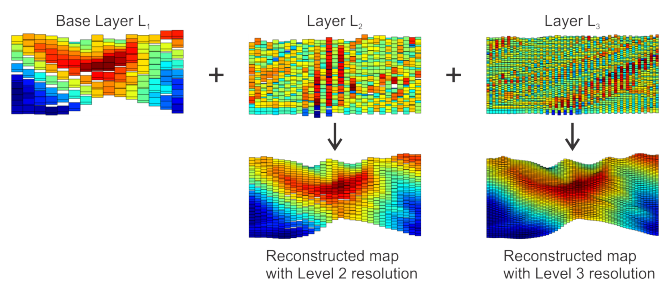


Figure 5. Map extraction at different resolutions.

6. FINDING SUITABLE LANDING SITES

Analyzing the Overflown Terrain

Several terrain features can become landing hazards to a rotorcraft. Depending on the design, especially of its landing gear, slopes and objects above a size limit will result in a non-stable landing or even result in damage or crash. We therefore evaluate the elevation map for slope, rock size, roughness, and confidence in the map reconstruction. The criteria for safe landing sites are:

- a *safe landing area* large enough to fit the vehicle plus a safety margin to establish a *keep-out zone* around landing hazards
- slope
- roughness, which includes discontinuities caused by rocks
- map reconstruction confidence

The landing site detector evaluates the elevation map in several stages. First, the local terrain slope - with respect to the *safe landing area* as a reference area - is calculated using a coarse map layer with a pixel footprint (resolution) that corresponds to the footprint of the vehicle. This reduces computational cost, while introducing only minimal error. Second, for areas that pass the slope test, the elevation map is derived at finer resolutions, and from coarse to fine, a roughness operator is applied to estimate terrain discontinuities within the landing area. The roughness operator considers two reference areas: the *safe landing area* itself, and a smaller *rock area* that depends on the desired minimum rock size (Figure 6). The roughness test fails, if the terrain deviates from a planar surface within the *safe landing area* which accounts for continuously sloping terrain, and if there are discontinuities beyond a threshold in a *rock area* within the safe landing area, accounting for abrupt changes around hazards. If a roughness test fails at a coarser level, the area is labeled as unsafe and no finer level is examined. Third, after processing each layer, a confidence test invalidates the detected landing area, if the map reconstruction confidence is below a threshold, again, aborting any further evaluation at a finer layer.

The areas that pass the landing site detection at the highest resolution available are designated as safe landing areas (e.g. the green area in Figure 8 and Figure 12) and annotated in a binary landing site map. Finally, a list of candidate landing sites is derived by selecting the center location of each landing area patch by applying a distance transform to the binary landing map and selecting the location with the maximum distance to any border as landing site.

To save computation time, the landing site detector is initiated by the on-board autonomy. The vehicle autonomy engine can either chose to receive a complete landing site list for the full image, or query a landing site for a specified region, if the vehicle needs to fly back to a previously detected landing site.

Searching for Landing Sites

In a notional autonomy architecture, the *Landing Site Detector* is complimented by a *Landing Behavior* (Figure 7). The landing behavior is responsible for querying the landing site detector and providing motion commands to a mobility layer, such as flying to a given waypoint above a selected landing site, and landing the vehicle. Additionally, the landing

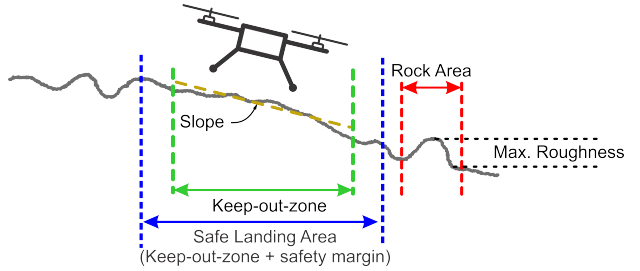


Figure 6. Landing site selection criteria. The *Safe Landing Area* includes the *keep-out-zone* required by the vehicle for safe landing, plus a safety margin to establish a safe distance to landing hazards.

behavior can survey and select a landing site.

The landing behavior and the landing site detector communicate through a query interface. This allows to decouple the landing site detection process from the mapping process within the landing site detector. 3D reconstruction and map aggregation is executed continuously, whereas the map evaluation is triggered by the behavior.

The landing behavior specifies a circle, with a lateral, X/Y location and radius for potential landing sites and the detector responds with a list of valid landing sites within the circular region, ordered by their proximity to the X/Y center location. In the case the detector cannot find a suitable landing site, it informs the landing behavior about the cause, which can be either because there is not sufficient data for a selection within the defined area, or there is sufficient data, but no valid landing site exists.

The landing behavior uses this interface to execute a landing maneuver in three distinct cases. In the first case, the landing behavior tries to land the vehicle at a pre-defined location. At a mission level, it is desirable to specify the landing site of the vehicle. For example, to support a multi-flight transit between two science locations. In this case, the behavior will first query the detector for landing sites near the desired landing site. If the vehicle has not yet flown over the desired area, it may be necessary for the behavior to survey the desired site. In a survey, the landing behavior flies the vehicle over the desired landing area at a low altitude to gather enough 3D measurements of the area to find suitable landing sites. For this purpose, the behavior moves throughout the landing area in a lawnmower pattern in order to collect elevation data over the entire desired landing area. It then re-queries the landing site detector for landing sites within the desired area. If no landing sites are found, it moves onto the second case.

In the second case, no valid landing sites are available in the desired area. Here, the behavior needs to select a landing

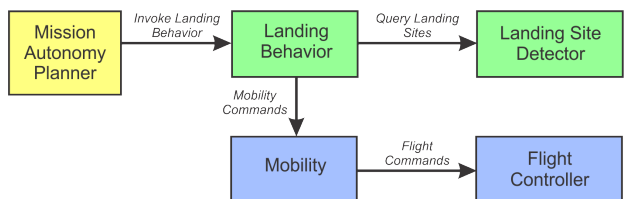


Figure 7. Notional architecture for a landing behavior.

site that has previously been seen during the flight up to this point, including the takeoff point. The behavior queries the detector about its current position with an increased, large radius. It then picks a landing site that is both likely to be valid and is within the remaining performance limits of the vehicle. From this point, the vehicle flies to the new landing site, re-evaluates it if necessary, and lands.

A final case involves an emergency landing. If the vehicle detects an anomalous condition - e.g. an unforeseen battery power drop - an immediate landing, even at a poor landing site, is preferable to crashing. In this case, the landing site behavior is triggered to request an emergency landing site from the landing site detector. The detector responds with the best landing site within reach, even if this site may not normally meet acceptability criteria, and the vehicle immediately navigates to it and lands.

7. EXPERIMENTAL EVALUATION

For verification and evaluation, we deployed our software in various scenarios in simulation and on data from UAS flights. We simulated flights of a Mars Helicopter over

Mars Victoria Crater using the JPL DARTS simulator [19] to validate the performance of 3D reconstruction under various noise scenarios, including noise overlays on generated images (shot noise and blur), and on IMU data (measurement noise and random walk).

Figure 8 illustrates a flight that passes over the crater rim using the DARTS simulator [19]. The flight was executed at 20 m altitude above ground to simulate a terrain following behavior. Tracked features are used by the state estimator and the camera pose refinement step. As can be seen, landing sites are correctly detected on flat terrain outside the crater, but not on the terrain below the rim that violates the slope constraint.

To verify the ability of the landing site detector to detect small landing hazard, we evaluated the detection results using simulated terrain with random rock distributions (Figure 9). Rocks with a random rock size were placed on a flat ground plane, and 3D reconstruction was simulated by producing a point cloud for a simulated camera (VGA resolution, 100° horizontal field of view) at each individual camera position directly from the terrain. Point clouds were overlaid with Gaussian noise corresponding to a 0.25 pixel disparity error for a fixed baseline between cameras of 4.8 m at a flight altitude between 5 m and 6 m.

The detection result for different rock sizes is shown in Figure 10. In this test, we perform a Monte-Carlo evaluation with randomly generated terrain for each flight. Rocks are distributed randomly over a ground plane and the flight trajectory is a straight line with random direction. Rock sizes were constant over one flight, but varied among different flights. Note, that we model rocks as half spheres with a height of half a diameter.

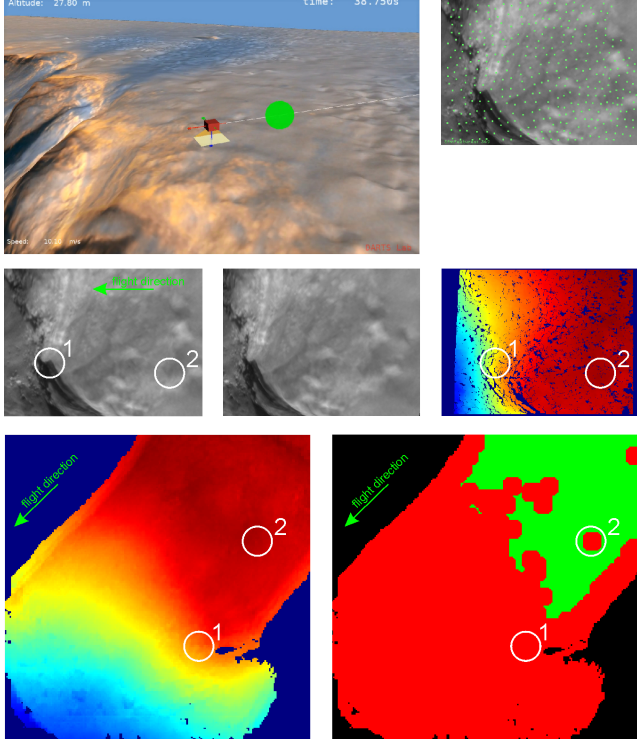


Figure 8. Flight in simulation environment. Top left: simulated UAS over Mars Victoria crater rim; Top right: current navigation camera image with overlaid tracked features; Middle from left to right: current reference view (rectified left image); past view (rectified right image); height map generated from stereo disparity map (warmer colors are closer to camera); Bottom left: aggregated elevation map (top-down view, note that map is rotated $\sim 45^\circ$); Bottom right: landing site map (green: safe landing site, red: landing hazard). White circles label selected landing hazards for visualization. Flight altitude: 20 m AGL. Map: 3 layers, 10 cm resolution at highest layer. Safety area radius: 1.0 m; slope threshold: 20° .

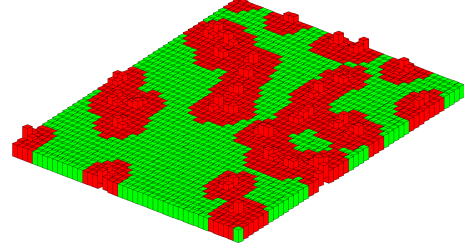


Figure 9. Landing site detection over simulated terrain with random rock distribution (detail). Green: safe landing location; Red: hazard location.

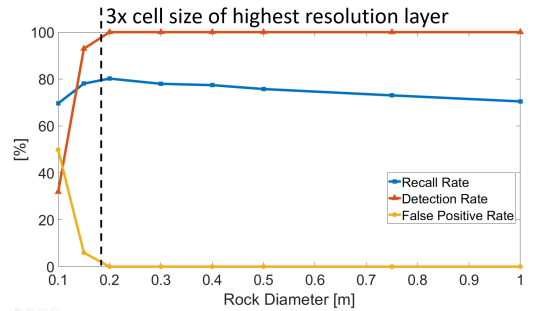


Figure 10. Rock detection rates using simulated terrain with random rock distribution. Flight altitude: 5-6 m; terrain slope: 5° . Map: 3 layers, 6 cm resolution at finest layer. Safety area radius: 0.7 m; keep-out zone radius used for evaluation: 0.5 m; slope threshold: 10° . Rocks are modelled as half spheres, with a rock height of half the rock diameter.

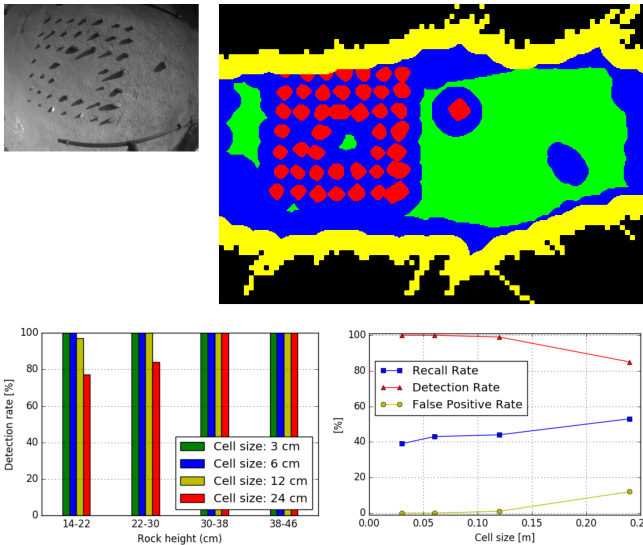


Figure 11. Landing site detection with UAS flight data over sample rocks: Top Left: Raw image of rock field used for evaluation. Top Right: Landing site map (green: safe landing site, blue: landing hazard, yellow: border region assumed to be hazardous, not evaluated, red: manually annotated landing hazard for evaluation). Bottom Left: Detection rate per rock height group for different map cell sizes. Bottom Right: Accumulated recall, detection, and false positive rate over different map cell sizes. Flight altitude: 5 m. Map: 3 layers. Safety area radius: 0.5 m, keep-out-zone radius used for evaluation: 0.3 m, slope threshold: 10°, rock area radius: 0.5 m, max. roughness: 0.1 m.

The *detection rate* corresponds to the number of rocks detected relative to the number of rocks that were visible to the simulated camera during flight - which is 100% if all visible rocks were detected. A rock counts as detected, if all map cells that contain a part of a rock plus a margin of half the keep-out-zone around the perimeter of the rock are labeled correctly as hazardous. *False positive rate* is the number of landing sites that are labeled as safe, but are unsafe in reality (false positives), relative to the total number of evaluated map cells with ground truth hazards (i.e. red cells in 9). Of course, the false positive rate should be zero to exclude crash landings. *Recall rate* is the number of map cells that are designated as safe landing sites, relative to the true number of safe landing sites - this would ideally be 100%, but the recall rate is usually traded against the false positive rate: We rather do not find all possible landing sites, if we can in turn reduce the *false positive rate* to zero. In our case, the recall rate is reduced by the added safety margin around the keep-out zone. As can be seen in Figure 10, the detector is able to resolve rock sizes larger than 3 times the cell resolution of the finest map layer with high accuracy.

We verified the simulation results with data from a UAS flight at 5 m altitude over an artificial rock field consisting of rocks with heights between 14 cm and 46 cm and evaluated the performance of the landing site detector for different map cell sizes (Figure 11). Images were collected with a nadir pointed camera with VGA resolution and approximately 110° horizontal field of view. As expected, the detection rate for smaller rocks decreases, if the cell size increases. This also leads to an increased false positive rate, since rocks are now missed. For this experiment, we selected rocks that roughly adhere to the half-sphere model, with a rock height of half

the rock diameter. As can be seen in Figure 11 the detection rate starts decreasing for cell sizes larger than $\sim 2/3$ the rock height, which agrees with the simulation results from Figure 10.

Figure 12 illustrates landing site detection with data from a UAS flight over an arid terrain. The top row shows the result of the 3D reconstruction process. On the bottom left, the aggregated map is shown in a top-down view, whereas the landing site map with safe landing sites labeled in green is shown on the bottom right. Note, that the map is rotated with respect to the reference view image by approximately 105°. The purple circles annotate selected landing hazards around a sandy patch of roughly 3 m diameter that includes a valid landing site (yellow circle), which is detected correctly by our software.

8. CONCLUSIONS AND FUTURE WORK

We introduced an advanced navigation module for a future Mars rotorcraft to autonomously detect landing hazards during flight. The proposed approach leverages existing sensor data and data processing products to minimize impact on size weight and power. The module was tested on various simulated and real environments, demonstrating the feasibility of a vision-based perception approach for safe landing site detection.

The landing site detection navigation module is currently being implemented on surrogate Mars Science Helicopter avionics hardware for on-board execution in near real-time with a target execution frame rate of 1 Hz. Once completed, we will verify and validate our approach during UAS flights over various Mars analog terrain types.

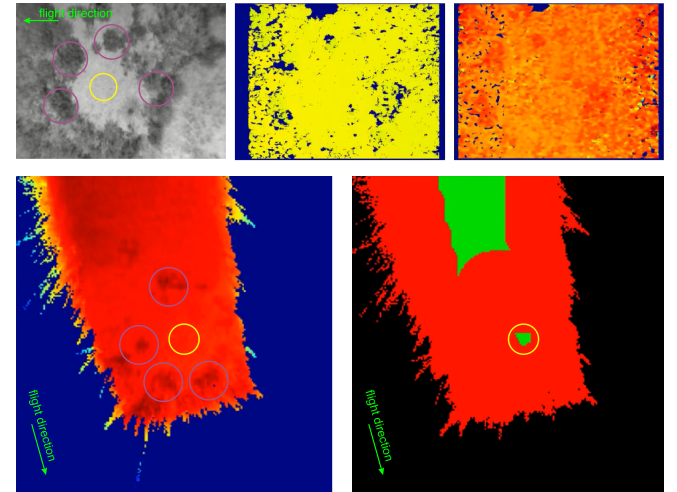


Figure 12. Landing site detection with UAS flight data: Top row: Left: Reference view (rectified); Middle: stereo disparity map; Right: height from range image. Bottom left: aggregated elevation map; Bottom right: landing site map (green: safe landing site, red: landing hazard). Purple circles label selected landing hazards for visualization. Yellow circle depicts suitable landing site on sand patch in input image. Note, that the map is rotated $\sim 105^\circ$. Flight altitude: 8 m. Map: 3 layers, 10 cm resolution at highest layer. Safety area radius: 1.0 m, slope threshold: 10°, rock area radius: 0.25 m, max. roughness: 0.1 m.

ACKNOWLEDGMENTS

The research was carried out at the Jet Propulsion Laboratory, California Institute of Technology, under a contract with the National Aeronautics and Space Administration (80NM0018D0004).

REFERENCES

- [1] J. Bapst *et al.*, “Mars science helicopter: Compelling science enabled by an aerial platform,” accessed: 2020-10-15. [Online]. Available: https://mepag.jpl.nasa.gov/reports/decadal2023-2032/MSH_whitepaper_draft_final_20copy.pdf
- [2] D. Bayard, D. Conway, R. Brockers, J. Delaune, L. Matthies, H. Grip, G. Merewether, T. Brown, and A. San Martin, “Vision-Based Navigation for the NASA Mars Helicopter,” in *AIAA Scitech Forum*, 2019.
- [3] J. Balaram, T. Canham, C. Duncan, M. Golombek, H. Grip, W. Johnson, J. Maki, A. Quon, R. Stern, and D. Zhu, “Mars Helicopter Technology Demonstrator,” in *AIAA Scitech Forum*, 2018.
- [4] H. Grip, J. Lam, D. Bayard, D. Conway, G. Singh, R. Brockers, J. Delaune, L. Matthies, C. Malpica, T. Brown, A. Jain, A. San Martin, and G. Merewether, “Flight Control System for NASA’s Mars Helicopter,” in *AIAA Scitech Forum*, 2019.
- [5] N. Trawny, A. Huertas, M. Luna, C. Villalpando, K. Martin, J. Carson, and A. Johnson, “Flight testing a real-time hazard detection system for safe lunar landing on the rocket-powered morpheus vehicle,” in *Proc. AIAA SciTech Conference*, 2015.
- [6] A. Johnson, N. Villaume, C. Umsted, A. Kourchians, D. Sternberg, N. Trawny, Y. Cheng, E. Giepel, and J. Montgomery, “The mars 2020 lander vision system field test,” in *Proc. AAS Guidance Navigation and Control Conference (AAS-20-105)*, 2020.
- [7] J. Engel, V. Koltun, and D. Cremers, “Direct sparse odometry,” *IEEE Transactions on Pattern Analysis and Machine Intelligence*, March 2018.
- [8] J. Engel, T. Schöps, and D. Cremers, “LSD-SLAM: Large-scale direct monocular SLAM,” in *European Conference on Computer Vision (ECCV)*, 2014.
- [9] V. Desaraju, N. Michael, M. Humenberger, R. Brockers, S. Weiss, J. Nash, and V. Matthies, “Vision based landing site evaluation and informed optimal trajectory,” *Autonomous Robots*, vol. 39, no. 3, 2015.
- [10] S. Daftry, M. Das, J. Delaune, C. Sorice, R. Hewitt, S. Reddy, D. Lytle, E. Gu, and L. Matthies, “Robust vision-based autonomous navigation, mapping and landing for MAVs at night,” in *ISER*, 2018.
- [11] R. Brockers, M. Humenberger, S. Weiss, and L. Matthies, “Towards autonomous navigation of miniature UAVs.” in *Embedded Vision Workshop at CVPR*, 2014.
- [12] A. Johnson, J. Montgomery, and L. Matthies, “Vision guided landing of an autonomous helicopter in hazardous terrain,” in *ICRA*, 2005.
- [13] C. Forster, M. Faessler, F. Fontana, M. Werlberger, and D. Scaramuzza, “Continuous on-board monocular-vision based elevation mapping applied to autonomous landing of micro aerial vehicles,” in *ICRA*, 2015.
- [14] J. Zienkiewicz, A. Tsotsios, A. Davison, and S. Leutenegger, “Monocular, real-time surface reconstruction using dynamic level of detail,” in *Fourth International Conference on 3D Vision (3DV)*, 2014.
- [15] T. Schneider, M. Dymczyk, M. Fehr, K. Egger, S. Lynen, I. Gilitschenski, and R. Siegwart, “An open framework for research in visual inertial mapping and localization,” *RA-L*, vol. 3, no. 3, 2018.
- [16] M. Pizzoli, C. Forster, and D. Scaramuzza, “Remode: Probabilistic, monocular dense reconstruction in real time,” in *ICRA*, 2014.
- [17] J. Delaune, R. Brockers, D. S. Bayard, H. Dor, R. Hewitt, J. Sawoniewicz, G. Kubiak, T. Tzanatos, L. Matthies, and J. Balaram, “Extended navigation capabilities for a future mars science helicopter concept,” in *IEEE Aerospace Conference*, 2020, pp. 1–10.
- [18] S. Goldberg, M. Maimone, and L. Matthies, “Stereo vision and rover navigation software for planetary exploration,” in *IEEE Aerospace Conference*, 2002.
- [19] A. Jain, “Darts - multibody modeling, simulation and analysis software.” in *Multibody Dynamics 2019*. Springer International Publishing, 2019, p. 433–441.

BIOGRAPHY



Roland Brockers is a Research Technologist at the Jet Propulsion Laboratory. He received his Ph.D. in Electrical Engineering from the University of Paderborn (Germany) in 2005, and has been conducting research in autonomous navigation of unmanned robotic systems for more than 20 years with a focus on aerial vehicles since 2010 where he worked on autonomous landing and ingress, visual pose estimation, and autonomous obstacle avoidance for micro air vehicles. Roland was part of the JPL Mars Helicopter GNC team and wrote the image-processing software for the Mars Helicopter flight project on Mars 2020. He is the PI of the Advanced Navigation for future Mars Rotorcraft R&D effort. His current research interests include 3D perception systems for small mobile robotic platforms, and autonomous robotic systems with applications in earth science and planetary exploration.



Jeff Delaune is a robotics technologist at the Jet Propulsion Laboratory. He researches and develops autonomous navigation and robotic systems for planetary exploration, with a focus on flying vehicles. Jeff was part of the navigation team for NASA’s Ingenuity Mars Helicopter flight project. His interests include state estimation, sensor fusion, perception, computer vision and mission design. Jeff received his Ph.D. in Robotics from Institut Supérieur de l’Aéronautique et de l’Espace (ISAE, France) in 2013, after a M.S. in Astronautics and Space Engineering from Cranfield University (United Kingdom), and a B.S./M.S. in Engineering from École Centrale de Nantes (France).



Pedro Proença is a Postdoctoral scholar at the Jet Propulsion Laboratory. He received his Ph.D. in Computer Vision from the University of Surrey (UK) in 2018, after a B.S and M.S. degree in Telecommunications and Computer Science from the ISCTE — University Institute of Lisbon (Portugal) in 2011 and 2013, respectively. His research interests include SLAM, 3D perception, deep learning and probabilistic modelling.



Pascal Schoppmann received a M.Sc. in Robotics, Systems and Controls from ETH Zurich in 2020. He has been with the Robotic Aerial Mobility Group at JPL for his Master thesis, where he worked on the topic of safe landing site detection for autonomous rotorcraft landing. Prior to JPL, he was a member of the academic racing team (AMZ) at ETH Zurich, responsible for various vehicle-dynamics control tasks and the perception system of an autonomous race car. During his study, he supervised a mechanical engineering group within the racing team developing a suspension system.



Matthias Domnik received a M.Eng. in information technology and electrical engineering from the University of Applied Sciences Dortmund in 2020. During his master's thesis he was associated with the Robotic Aerial Mobility Group at the Jet Propulsion Laboratory in Pasadena, CA. In 2017, Matthias received a B.Eng. degree in automotive engineering from the University of Applied Sciences Dortmund.



Gerik Kubiak received his B.S. degree in Computer Engineering in 2016 from the California Polytechnic State University – San Luis Obispo. He currently works as a robotics systems engineer for the Mars 2020 Robotics Arm. Previously he worked on software and operations for the Mars Helicopter flight project. His interests include embedded systems and robotics.



Theodore Tzanatos received his B.S. degree in Electrical Engineering and Computer Science in 2012 and a M.Eng. in Electrical Engineering and Computer Science from the Massachusetts Institute of Technology in 2013. He is currently a test conductor for the Mars Helicopter flight project on Mars 2020 and PI for the Mars Science Helicopter System R&D effort. His interests include embedded systems, aerial vehicles, and autonomy.